Deep-Sea Research I 69 (2012) 62–69

Contents lists available at SciVerse ScienceDirect

Deep-Sea Research I

journal homepage: www.elsevier.com/locate/dsri

On eddy polarity distribution in the southwestern Atlantic

Martin Saraceno [a,*], Christine Provost [b]

[a] Centro de Investigaciones del Mar y la Atmósfera, CIMA/CONICET-UBA, DCAO/FCEN-UBA, UMI-IFAECI/CNRS-CONICET-UBA, Ciudad Universitaria, Pabellón II Piso 2, C1428EHA, Ciudad Autónoma de Buenos Aires, Argentina

[b] Laboratoire d'Océanographie et du Climat: Expérimentation et Approche Numérique (LOCEAN), UMR 7159, Université Pierre et Marie Curie, T 45-46, 5E, 4 place Jussieu, 75005 Paris, France

ARTICLE INFO

Article history:
Received 27 March 2012
Received in revised form
6 July 2012
Accepted 11 July 2012
Available online 25 July 2012

Keywords:
Eddies
Southwestern Atlantic
Zapiola Drift

ABSTRACT

Eddies in the southwestern Atlantic were detected from more than 18 years of satellite altimetry data using a modified version of the Okubo–Weiss method. The spatial distribution and polarity of eddies were examined. A larger concentration of cyclonic (anticyclonic) eddies was found on the left (right) side when looking downstream on some of the largest current systems in the region, such as the South Atlantic Current, the anticyclonic circulation associated with the Zapiola Drift (ZD) and the northern branch of the Antarctic Circumpolar Current. In the region isolated by the anticyclonic Zapiola Current, 91% of eddies were cyclonic. The observed distribution of eddies is in agreement with the generation of eddies from meanders of the above-mentioned currents: cyclonic (anticyclonic) eddies might detach from a meander of the current on the left (right) side when looking downstream on the current. Furthermore, in the ZD area, the bottom topography plays a key role in determining the trajectory of eddies: the anticyclonic current associated with the ZD meanders and eventually generates a cyclonic eddy that enters the ZD region only across the northeastern border, where the gradient of potential vorticity is lower. Finally, average surface chlorophyll-*a* concentration inside cyclonic and anticyclonic eddies shows that the former have higher chlorophyll-*a* values. Thus, on average, the classical eddy-pumping theory explains the difference in chlorophyll-*a* concentration within eddies in the southwestern Atlantic.

1. Introduction

Eddies are important to all aspects of oceanography and often involve the overlap of research areas such as physical and biogeochemical oceanography. From a physical point of view their importance resides in the fact that they play an important part in the mixing processes in the surface layer of the ocean and for transporting energy, like heat. Eddies can contribute significantly to the transfer of the temperature and salinity characteristics of one region to another, very different, region. Thus they play an important role in the meridional overturning circulation, the strength of which is a key parameter for monitoring and predicting climate change (e.g., Mazloff et al., 2010; Farneti et al., 2010). From a biogeochemical point of view, cold-core (cyclonic) eddies bring nutrients to the surface which become available for photosynthesis. Hence, they can fertilize the upper ocean to support phytoplankton blooms. Eddies also play an important ecological role, since they can trap, transport and disperse different communities of organisms. Thus, eddies play a crucial role at regional and global scales in several domains. Improving the knowledge of the spatial distribution and polarity of eddies will contribute to a better understanding of their role in the ocean.

In the southwestern Atlantic (SWA), the eddy kinetic energy can be as high as 1700 $cm^2\,s^{-2}$ (Fig. 1). The confluence of the Malvinas Current (MC) and the Brazil Current (BC) near 38°S, forms the Brazil/Malvinas Confluence region (BMC, hereafter), one of the most energetic regions of the world ocean (Gordon, 1981; Chelton et al., 1990). The meanders, eddies and filaments in the BMC are extraordinary in terms of their shape, size and abundance compared to other regions of the ocean. High-resolution images of sea surface temperature (SST) and chlorophyll-*a* concentration suggest that the associated mesoscale processes enhance the productivity in the region (e.g., Barré et al., 2006; Saraceno et al., 2005).

The BMC is characterized by the confluence of the Subantarctic Front (SAF) and the Subtropical Front (STF), which are, respectively, the northern limit of the subantarctic waters and the southern limit of the subtropical waters. The region where the SAF and STF merge at about 39°S is usually referred to as the Brazil/Malvinas front (e.g., Saraceno et al., 2004). A scheme of the upper circulation of the region, including the position of

* Corresponding author.
E-mail address: saraceno@cima.fcen.uba.ar (M. Saraceno).

0967-0637/$ - see front matter © 2012 Elsevier Ltd. All rights reserved.
http://dx.doi.org/10.1016/j.dsr.2012.07.005

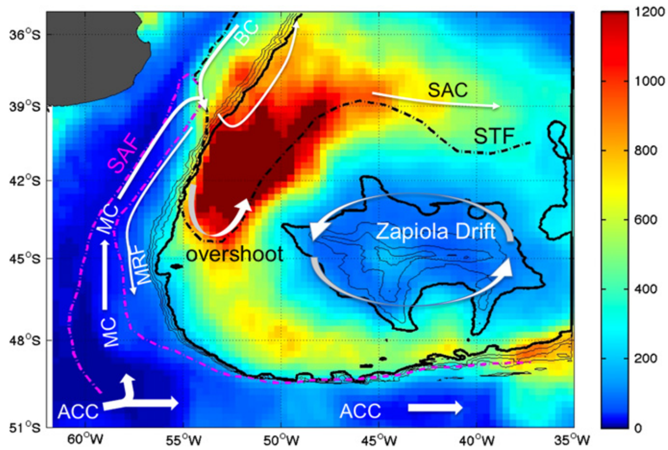

Fig. 1. Colors indicate the *EKE* values (units $cm^2\,s^{-2}$) of sea-level anomalies for the period 1992–2010 estimated from satellite altimetry data (see text for details of the dataset). *Black lines* indicate potential vorticity isolines (units $-1\times10^{-8}\,m^{-1}\,s^{-1}$) and range from $-2.1\times10^{-8}\,m^{-1}\,s^{-1}$ to $-1.92\times10^{-8}\,m^{-1}\,s^{-1}$. The *boldface* closed potential vorticity contour centred at 43°W, 45°S corresponds to the $-1.92\times10^{-8}\,m^{-1}\,s^{-1}$ value and is used to represent the Zapiola Drift area (Saraceno et al., 2009). The mean positions of the Subtropical Front (STF) and the Subantarctic Front (SAF) are from Saraceno et al. (2004) and are indicated by *black* and *magenta dash-dotted lines*, respectively. Representative positions of the Brazil Current (BC), Malvinas Current (MC), Malvinas Return Flow (MRF), Antarctic Circumpolar Current (ACC), South Atlantic Current (SAC) and overshoot region are indicated. (For interpretation of the references to color in this figure legend, the reader is referred to the web version of this article.)

these fronts, is shown in Fig. 1. The MC is part of the northern branch of the Antarctic Circumpolar Current (ACC), which carries the cold (<7 °C at the surface in winter) and relatively fresh Subantarctic Mode Water (SAMW) equatorwards along the western edge of the Argentine continental shelf. The BC flows polewards along the continental margin of South America as part of the western boundary current of the South Atlantic subtropical gyre. It transports the warm (higher than 26 °C at the surface) and salty South Atlantic Central Water (SACW). After its confluence with the MC, the BC separates into two branches (Peterson and Stramma, 1991). One branch turns to the north forming a recirculation cell while the other branch flows southwards and returns northeastwards at about 44°S. This second branch is commonly referred to as the overshoot of the Brazil Current and, east of 45°W, it forms the South Atlantic Current (Peterson and Stramma, 1991). After the collision with the BC, the main flow of the MC describes a sharp loop forming the Malvinas return flow. The Malvinas return flow flows southwards and turns eastwards at 49°S.

Further towards the center of the South Atlantic, an important feature that affects the large-scale circulation is the presence of a large zonal sedimentary deposit known as the Zapiola Drift (ZD). The effect of this submarine feature on the surface of the ocean is clearly observed in the satellite images of SST, SST gradient, chlorophyll-*a* and sea surface height (SSH) (Saraceno et al., 2005). The anticyclonic circulation around the ZD is eddy-driven (Dewar, 1998). A meridional transport of 80 Sverdrups (1 Sverdrup$=10^6\,m^3\,s^{-1}$) on the western and eastern flanks of the ZD with southgoing and northgoing currents, respectively, of about equal magnitude, has been estimated from in situ measurements during the WOCE A11 cruise (Saunders and King, 1995b). Satellite altimetry data (Saraceno et al., 2009) and model outputs (Bigorre and Dewar, 2009; Venaille et al., 2011) suggest that the anticyclonic circulation associated with the ZD is characterized by an important interannual variability. Despite the importance of eddies in the ZD circulation, a precise description of the interaction between eddies and the anticyclonic circulation has not been provided yet.

Eddies have been detected in the southwestern Atlantic since the first global satellite infrared images of SST were acquired (Legeckis and Gordon, 1982). Despite their high spatial resolution, sea surface temperature (SST) images are limited by the cloud coverage. In contrast, satellite radar altimetry sensors provide "cloud-free" SSH images. Using a combination of along-track SSH, climatological temperature and salinity fields, Lentini et al. (2006) showed that 40 warm-core eddies were released by the BC in the period 1993–1998. Analysis of gridded SSH maps suggested that a much larger number of eddies is present in the region (Saraceno, 2010). Mesoscale surface circulation can be accurately estimated from SSH data when two or more satellite missions are used to construct gridded fields (Pascual et al., 2006; Chelton et al., 2011a). Thus, gridded maps of SSH data are particularly useful in the study of mesoscale structures and of the interaction between mean currents and eddies in the ocean. Several studies have therefore used satellite SSH data to detect and track eddies in the ocean (e.g., Chaigneau et al., 2008, 2009; Chelton et al., 2011a).

We took advantage of the 18-year-long altimetry time-series to detect eddies and track them in the southwestern Atlantic. We used one of the most popular techniques to detect eddies, the Okubo–Weiss (OW) algorithm (Okubo, 1970; Weiss, 1991; Isern-Fontanet et al., 2003). The OW algorithm is based on physical criteria, whereas other methods of eddy detection are more geometrical. Because of the complex nature of the flow field in the southwestern Atlantic and in order to distinguish eddies from meanders we had to modify the OW method slightly. We validated the modified method and then applied it to the whole altimetry time-series. We examined the distribution of eddies and of eddy polarity and discuss their relation with the circulation in the region.

The article is organized as follows. Section 2 provides a brief description of the datasets. The methodology and the validation strategy are explained in Section 3. Section 4 presents and discusses the results. Section 5 summarizes the results and outlines perspectives.

2. Data

2.1. Satellite sea-level anomaly

We used the reference, delayed time-series of the gridded data fields of sea level anomaly (SLA) produced by Ssalto/Duacs and distributed by AVISO (http://www.aviso.oceanobs.com). SLA AVISO fields are computed with reference to a mean for the period 1993–1999. We extracted the gridded data fields of SLA for the region of interest (60°W–35°W, 50°S–35°S) from the global SLA fields for the period 14 October 1992–1 December 2010 (18+ years).

Satellite altimetry missions have accurately determined sea surface height (SSH) since the launch of the TOPEX/Poseidon (T/P) satellite in 1992 (Fu and Cazenave, 2001). Six satellite altimetry missions (Jason-1, ERS-1, ERS-2, Envisat, GFO and Jason-2) have been launched since then. The processing of along-track data from the altimetric missions into gridded fields of SSH was described by Le Traon et al. (2003). The reference time-series always uses two contemporary satellite missions to construct the interpolated SSH fields: one in a 10-day repeat orbit (T/P, followed by Jason-1 and Jason-2) and another one in a 35-day repeat orbit (ERS-1, followed by ERS-2 and Envisat). The time-series is produced weekly on a $1/3°\times1/3°$ grid in a Mercator projection. The objective procedure to obtain the gridded fields of SSH by AVISO includes a spatial filtering that has half-power filter cut-off wavelengths of about 2° in latitude and 2° in longitude, which corresponds to an e-folding radius of about 0.4°, or about 40 km at mid-latitudes (Chelton et al., 2011a). The dataset can then be used to detect eddies whose radii are larger than 40 km. We only considered eddies detected offshore in depths greater than 200 m. Indeed, intrinsic difficulties affect the corrections applied to the altimeter data on the Patagonian shelf (e.g., wet tropospheric component, tidal component) and data are usually flagged as unreliable within a certain distance of the coast. Moreover, the interpolation of along-track data provides only marginal resolution of high-frequency and small-scale structures which are abundant on the Patagonian shelf (Acha et al., 2004).

2.2. SeaWiFS-derived chlorophyll-a concentrations

Near-surface chlorophyll-*a* concentrations used in this study consist of 8-day, 9-km gridded estimates derived from satellite measurements of ocean color by the Sea-viewing Wide Field-of-view Sensor (SeaWiFS) (McClain et al., 1998) using the Garver–Siegel–Maritorena (GSM) semi-analytical ocean color algorithm (Garver and Siegel, 1997; Maritorena et al., 2002). These chlorophyll-*a* concentration fields are available online at ftp://ftp.oceancolor.ucsb.edu/pub/org/oceancolor/MEaSUREs/Seawifs/. Despite the fact that cloud cover places a strong limitation on this dataset, the composite average minimizes the cloud-cover problem and keeps a reasonable time resolution to allow detection of mesoscale features in the ocean surface layer. Color images are used in the validation strategy described in Section 3.3 and to composite chlorophyll-*a* concentrations within eddies of the same polarity. The most common explanation for the different chlorophyll-*a* concentration in the eddy interior is that the geostrophic adjustment required to maintain the circulation implies a thermocline rise inside the cyclonic eddies and a depression in the anticyclonic eddy. When the nutricline and the thermocline are coincident, then enhanced production is expected within cyclonic eddies. However this simple explanation has its shortcomings: complex non-linear biophysical dynamics control the phytoplankton growth, which depends on the critical balance of stirring, mixed-layer depth, stability of the water column, temperature and availability of light.

2.3. Surface-buoy trajectories

Satellite-tracked drifter data used in this work are part of the global data set available from the Drifter Data Assembly Center (DAC) at the National Oceanographic and Atmospheric Administration's Atlantic Oceanographic and Meteorological Laboratory (NOAA/AOML). The data set is public and can be downloaded from AOML's ftp server (ftp://ftp.aoml.noaa.gov/phod/pub/buoydata).

Quality control at DAC involves the interpolation of the raw fixes (16 to 20 satellite fixes per day per drifter) uniformly at six-hour intervals using a kriging interpolation scheme (Hansen and Poulain, 1996). The data from drifters with no drogue attached were discarded, as were all interpolated positions with an uncertainty greater than 1 km. The remaining trajectories were low-pass-filtered with a 2-day Gaussian filter in order to remove tidal fluctuations and other high-frequency variability of no interest in the present study. The Ekman component, estimated following Ralph and Niiler (1999), was excluded: in the region under consideration, the estimated Ekman velocity is similar to the velocity uncertainty (less than 1 cm s^{-1}, even with strong winds).

3. Methodology

3.1. Eddy-detection

The Okubo–Weiss method may be summarized as follows. First, surface velocities are estimated from SLA following the geostrophic approximation:

$$v = \frac{g}{f}\frac{\partial \eta}{\partial x} \tag{1}$$

$$u = -\frac{g}{f}\frac{\partial \eta}{\partial y} \tag{2}$$

where u and v are, respectively, the zonal and meridional geostrophic surface velocity components, η is SLA, g is the gravity and f is the Coriolis factor. The relative vorticity (ω), normal strain (S_n) and shear strain (S_s) deformation rates can then be computed:

$$\omega = v_x - u_y \tag{3}$$

$$S_n = u_x - v_y \tag{4}$$

$$S_s = v_x + u_y \tag{5}$$

The Okubo–Weiss parameter (W) can be then computed as:

$$W = S_n^2 + S_s^2 - \omega^2 \tag{6}$$

W was developed first by Okubo (1970) and later by Weiss (1991); the automatization of the method was first implemented by Isern-Fontanet et al. (2003). The method identifies regions of the flow where the relative vorticity component dominates the strain tensors, defined as the center of the eddy. Considering horizontally non-divergent flows, i.e., where $u_x + v_y = 0$, Eq. (6) simplifies to:

$$W = 4(v_x u_y + u_x^2) \tag{7}$$

Eddies are identified as the regions where $W < b\sigma$, σ being the standard deviation of the geostrophic velocity field at each time, b being a constant value. We used a value for b that has been successfully used in several regions: 0.2 (Chaigneau et al., 2008).

Results (not shown) obtained with the classical OW algorithm described above indicated that several eddies were identified in regions where non-closed contours of SLA were present. This happens in regions where a strong curvature of the geostrophic velocities exists; i.e., where strong meanders are present. The Brazil/Malvinas Confluence and overshoot regions are the two regions where most of the eddies corresponding to non-closed contours were detected. To overcome this difficulty we adopted the following strategy: Once we obtained the center of the eddy by applying the OW algorithm described above, we looked for the corresponding SLA value and searched for the highest (lowest) closed contour for cyclonic (anticyclonic) eddies. The center of the eddy was then re-estimated based on the new contour. We stopped the algorithm when one of the following two conditions first arose: (i) the length of the eddy contour was larger than the previous one by more than 7 pixels; (ii) the distance between any pair of points within the contour considered must be less than 400 km. These two conditions avoid cases of multiple centers and preserve the usual notion of a compact form for rotating vortices. The second condition is the same as in Chelton et al. (2011a). We then estimated the amplitude of each eddy as the absolute difference between the SLA at the center of the eddy and the average of the SLA at the corresponding contour. We considered only eddies with amplitudes greater than 2 cm. The 2-cm threshold was chosen after a sensitivity study (Section 3.3).

The simple technique described above combines the physical criteria of the OW method with the conventional geometric definition of an eddy as a closed contour of SLA.

3.2. Eddy tracking

The eddy-tracking algorithm was adapted from Penven et al. (2005) and follows the approach used by Chaigneau et al. (2008). The method minimizes a distance D between the detected eddies of two consecutive maps. For each eddy ($e1$) identified on a given map at time $t1$ and for each eddy ($e2$) identified on the next map at time $t2$ and rotating in the same sense as $e1$, the non-dimensional distance $D_{e1;e2}$ is defined as:

$$D_{e1;e2} = \sqrt{\left(\frac{\Delta D}{D_0}\right)^2 + \left(\frac{\Delta R}{R_0}\right)^2 + \left(\frac{\Delta \mu}{\mu_0}\right)^2 + \left(\frac{\Delta EKE}{EKE_0}\right)^2} \quad (8)$$

where ΔD is the spatial distance between $e1$ and $e2$, and ΔR, $\Delta \mu$ and ΔEKE are, respectively, the radius, the vorticity and the eddy kinetic energy (EKE) differences between $e1$ and $e2$. D_0, R_0, μ_0 and EKE_0 are, respectively, the characteristic length scale ($D_0 = 100$ km), the characteristic radius ($R_0 = 50$ km), the characteristic vorticity ($\mu_0 = 10^{-6}\,\mathrm{s}^{-1}$) and the characteristic EKE ($EKE_0 = 100\,\mathrm{cm}^2\,\mathrm{s}^{-2}$). $D_{e1;e2}$ represents the degree of similarity between two eddies (the smaller the value, the higher the similarity between $e1$ and $e2$). Thus, the algorithm selects the eddy pair ($e1$, $e2$) that minimizes $D_{e1;e2}$ and considers this pair to be the same eddy that is tracked from $t1$ to $t2$. To avoid jumping from one track to another, the search distance, ΔD, was restricted to 150 km. Eddies may also disappear between consecutive maps, particularly if they pass into the gaps between satellite ground tracks. To minimize this problem, we searched for the same eddy for two weeks after its disappearance.

3.3. Validation strategy

To determine the accuracy of the methodology described above we applied an objective validation protocol similar to the one described by Chaigneau et al. (2008). The location and number of eddies detected with the modified OW method were compared with the location and number of eddies detected by two different methods, one using drifting buoys (method A1), the other using composite images of chlorophyll-*a* concentration and SLA (method B1). The two methods are described below. An example illustrating eddies detected by the three methods (modified OW, A1 and B1) is shown in Fig. 2.

3.3.1. Method A1: Eddy detection using drifting buoys

We selected buoy trajectories that clearly showed loops suggesting eddy-trapping, that is trajectories that made more than two complete loops (clockwise or anticlockwise) in a

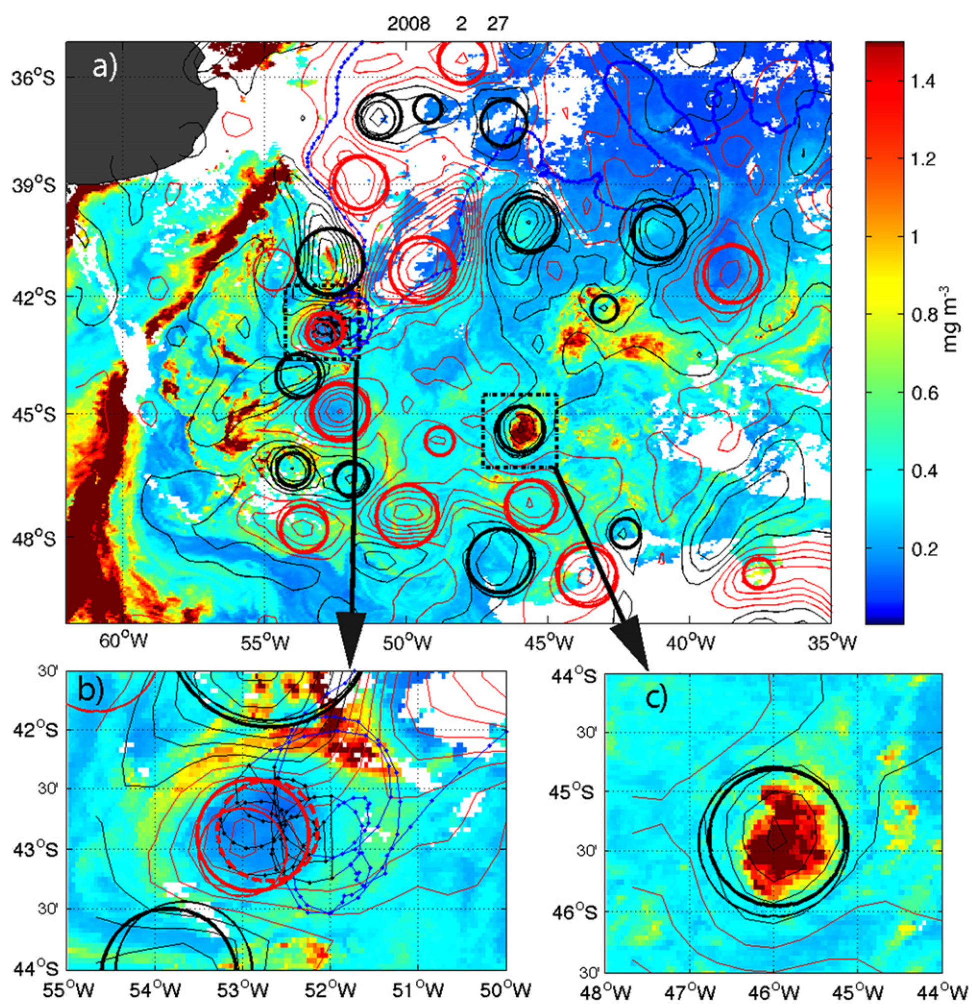

Fig. 2. (a) chlorophyll-*a* concentration (mg m^{-3}) in the background; *thin black* and *red contour lines* are SLA isolines contoured every 10 cm from −100 cm to 0 cm and from +10 cm to +150 cm; the *blue dotted line* is the trajectory of the buoy 2529260. (b) and (c) are enlarged regions from (a). *Black* (*red*) *circles* correspond to the cyclonic (anticyclonic) eddies detected by the OW method (*boldfaced-line circles*), method A1 (*dashed-line circle*, see panel (b) and method B1 (*thin-line circles*). On panel (b), *black dots* correspond to the part of the buoy trajectory considered to compute the date of the SLA and chlorophyll-*a* concentration images displayed (27 February 2008). Colorbar on the right refers to the background chlorophyll-*a* concentration field and is common to the three panels. (For interpretation of the references to color in this figure legend, the reader is referred to the web version of this article.)

geographical region no larger than 3° by 3°. This way, 52 trajectories were selected. For each section of the trajectory considered as corresponding to an eddy, the center and radius were computed taking into account the positions of the buoy in the region where the buoy made at least two complete loops. The center was estimated as the intersection of the average latitude and longitude of the selected buoy positions. The radius was estimated as half of the largest distance between positions.

3.3.2. *Method B1: Eddy detection using images of chlorophyll-a concentration and SLA*

Ten randomly selected maps of SLA were used in combination with the corresponding chlorophyll-*a* concentration images. An example is shown in Fig. 2. We chose the center and radius of each vortex present in the ten composite images by a careful inspection of the closed contours of SLA and the spatial distribution of chlorophyll-*a* concentration. Each composite image was displayed in a PC screen and using an interactive program we selected the center and radius of each eddy. We repeated the procedure separately for cyclonic and anticyclonic eddies.

3.3.3. *Comparison strategy*

To quantify the differences between the number of eddies detected by methods A1 and B1 with those detected by the modified OW method, we computed, for the cyclonic and anticyclonic eddies separately, the intersection and complementary areas of each eddy. If the intersection area was larger than 50% of the complementary area, we considered the eddy detection to be correct. A sensitivity study (results not shown) in which we modified the radius and position of two overlapping eddies showed us that the 50% value is a good choice for the correct detection of eddies whose radii do not differ by more than 50% and for which the distance between the centers is shorter than the average of the two eddies' radii.

While method A1 could only be used to compare 52 eddies, we counted a total of 223 eddies in the 10 images selected at random (method B1). Results are presented in Section 4.1.

4. Results

4.1. *Validation*

As discussed in the data Section 2.1, we do not consider the continental platform. The total number of eddies detected by each method (A1, B1, OW) and their polarity, whether cyclonic or anticyclonic, are reported in Table 1.

According to the criteria defined in Section 3.3.3, of the 52 eddies detected using method A1 (drifting buoys), 42 matched those detected by the OW method, leading to a 81% agreement between the A1 and OW methods.

The B1 method (composite color images and SLA maps) and the OW method detected 223 and 264 eddies, respectively, in the 10 randomly selected images that lead to an agreement of 80% between the A1 and OW methods. Inspection of the 41 mismatched eddies showed that they were randomly distributed and equally proportioned between cyclonic and anticyclonic ones. On the other hand, methods B1 and OW both gave a slightly larger number of cyclonic than anticyclonic eddies (Table 1).

Table 1
Cyclonic, anticyclonic and total number of eddies detected by methods A1, B1 and the modified OW.

Method	Cyclonic	Anticyclonic	Total
A1	23	29	52
B1	118	105	223
OW	137	127	264

Thus, the comparison of the OW method with methods A1 and B1 suggests that the uncertainty associated with the automated eddy-detection methodology used in this work is less than 20%. Detecting eddies with amplitudes smaller than 2 cm led to larger differences between the methods, so we kept the 2-cm threshold, which corresponds to the accuracy of SLA maps. We consider that the modified OW method is validated and applied it to the entire altimetric time series.

4.2. *Eddy distribution*

Fig. 3 shows the distribution of cyclonic (C) and anticyclonic (A) eddies in the southwestern Atlantic. First, there are more C than A eddies inside the area defined by the ZD. In the rectangular box contained inside the longest potential vorticity contour that encloses the ZD (see Fig. 3), the number of C eddies is 10 times greater than the number of A eddies (182 and 18, respectively, for the period considered). On the other hand, just outside the ZD, the number of A eddies (236) is greater than the number of C eddies (180). The region defined as outside the ZD was estimated as a

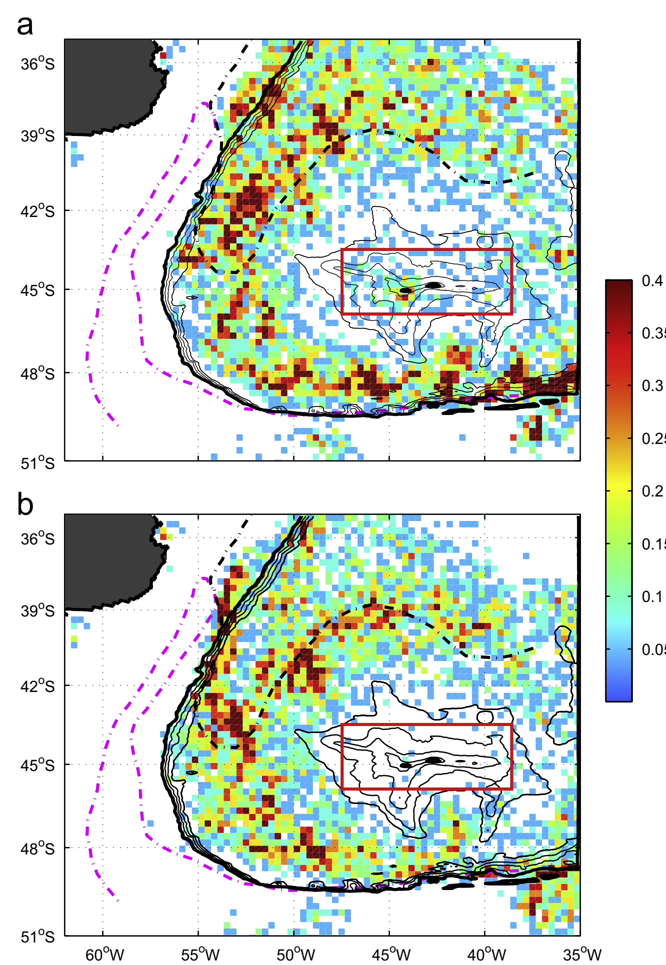

Fig. 3. Normalized spatial distribution of the concentration of cyclonic (*panel a*) and anticyclonic (*panel b*) eddies in the SWA. The total number of eddies whose centers fall in the area of a given pixel is divided by the largest common value (36). *Black* and *magenta lines* are as in Fig. 1 except for the *boldface black line* which here corresponds to the $-2.1 \times 10^{-8}\,m^{-1}\,s^{-1}$ potential vorticity contour. The *red line* corresponds to the area considered in the count of the number of A and C eddies inside the ZD. (For interpretation of the references to color in this figure legend, the reader is referred to the web version of this article.)

one-degree margin that follows the closed potential vorticity contour depicted in Fig. 3. The two results described above are compatible with the following explanation, schematically shown in Fig. 4. The ZD is a dynamically isolated region (Dewar, 1998; Saraceno et al., 2005, 2009) which is contoured by an A circulation. We propose that eddies that can enter the ZD isolated area are detachments attributable to meanders in the A circulation associated with the ZD (Fig. 4). This mechanism may also explain why the number of A eddies is higher than the number of C eddies just outside the ZD area. The eddy-formation mechanism is the same as that used to explain the formation of A (C) eddies north (south) of the Gulf Stream in the North Atlantic (e.g., Schmitz and Holland, 1982).

Second, as expected, the number of eddies is maximum in regions where the EKE is higher, such as the BMC region or the region between the SAF and the ZD, south of 46°S (Figs. 1 and 3). C eddies are more numerous north of the STF, while A eddies are more numerous along or south of the STF (Fig. 3). Meanders of the BC and the consequent generation of A (C) eddies south (north) of the mean position of the STF is a potential mechanism explaining the distribution of eddies in the BMC region. Detachments of eddies from meanders of the Antarctic Circumpolar Current (ACC), which flows westwards along the SAF, may also explain the larger concentration of C eddies north of the SAF between 50°W and 35°W (Fig. 3). However, a larger concentration of A eddies south of the SAF is not observed. Two spots centered approximately at 50°S, 48°W and 50°S, 37°W with a significant number of eddies (both C and A) are located south of the SAF and correspond to regions where the sea floor is shallower than it is in the surrounding regions, enhancing the formation of meanders and eddies. This is also reflected by large values of *EKE* (Fig. 1).

Third, eddies are mostly observed within the region with potential vorticity larger than $-2.1\times10^{-8}\,\mathrm{m}^{-1}\,\mathrm{s}^{-1}$ (Fig. 3). Indeed, the $-2.1\times10^{-8}\,\mathrm{m}^{-1}\,\mathrm{s}^{-1}$ potential vorticity contour appears as a barrier for eddies except for the two locations south of the SAF mentioned above and for the region north of Brazil/Malvinas front. The modified OW algorithm did not find eddies either in the MC itself or in the Malvinas return-flow area. Evidently, the Brazil/Malvinas front is a barrier for eddies. The position of the Brazil/Malvinas front, indicated in Fig. 3, has been estimated from infrared sea surface temperature images (Saraceno et al., 2004), hence a completely independent dataset.

Fourth, there is a local maximum in the number of C eddies centered just over the top of the ZD; that is, where the ZD reaches its maximum height (see Fig. 3 at 44.5°W, 45.5°S). This can be explained by considering that, once C eddies are generated inside the ZD area, the bottom topography favors their location over the top of the ZD: assuming that bottom friction is weak, the conservation of potential vorticity implies that a vorticity anomaly travelling upslope would need to decrease its relative vorticity (neglecting the *beta* effect for simplicity), so that anticyclones would weaken, whereas cyclones would be reinforced on their way towards the peak of the ZD.

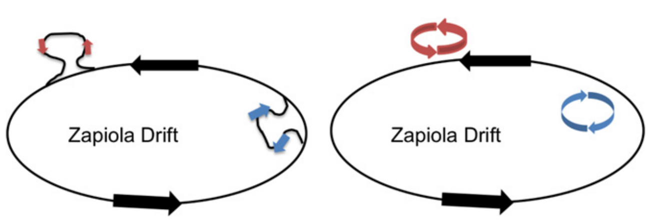

Fig. 4. Schematic representation of the mechanism proposed to explain the larger number of C (A) eddies inside (outside) the ZD area. *Left panel*: The anticyclonic Zapiola Current (*black arrows*) may generate meanders inside (loop with *blue arrows*) and outside the ZD (loop with *red arrows*). *Right panel*: meanders may eventually separate from the main current, creating a C eddy (*blue arrows*) inside the ZD area and an A eddy (*red arrows*) outside the ZD area. (For interpretation of the references to color in this figure legend, the reader is referred to the web version of this article.)

Finally, comparison of potential vorticity contours (Fig. 5) with the trajectories of the C and A eddies that we could follow for more than 6 weeks (Fig. 6) also suggests a relevant observation: most of the C eddies that enter the ZD region did so from the northeastern flank. This is the region where the slope of the potential vorticity contours is less pronounced (Fig. 6). It is therefore more likely that the A current associated with the ZD is able to meander more vigorously in this region or, in other words, is less controlled by the topographic gradient that defines the ZD. As a consequence, C eddies generated as illustrated in Fig. 4 enter the ZD area more frequently on the northeastern flank of the ZD region.

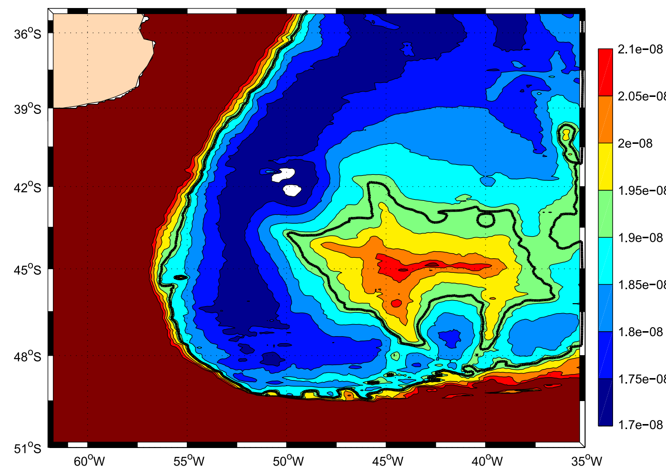

Fig. 5. Potential vorticity contours (units $-1\times10^{-8}\,\mathrm{m}^{-1}\,\mathrm{s}^{-1}$). *Boldface black line* corresponds to the $-1.92\times10^{-8}\,\mathrm{m}^{-1}\,\mathrm{s}^{-1}$ contour.

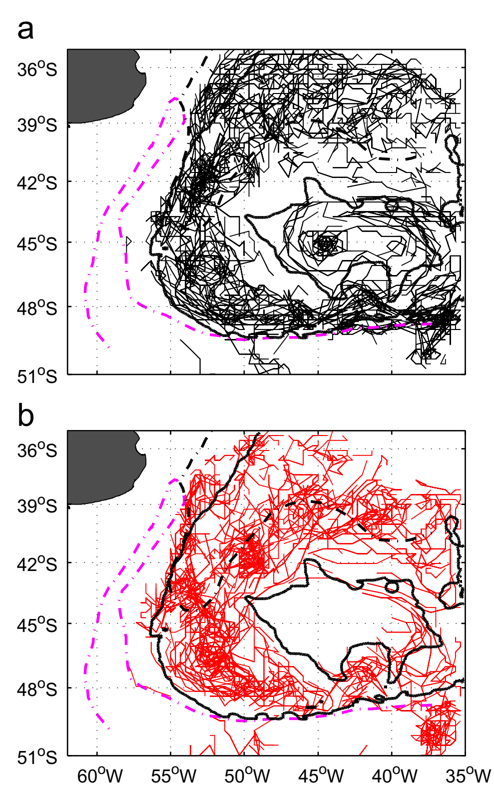

Fig. 6. Trajectories corresponding to the cyclonic (*panel a*) and anticyclonic (*panel b*) eddies detected. SAF and STF are represented by *magenta* and *black dash-dotted* lines, respectively. The potential vorticity contour $-1.92\times10^{-8}\,\mathrm{m}^{-1}\,\mathrm{s}^{-1}$ is plotted with a *boldface black line*. (For interpretation of the references to color in this figure legend, the reader is referred to the web version of this article.)

4.3. Temporal evolution of cyclonic eddies inside the Zapiola Drift area

The time-series of the number of C eddies inside the ZD area suggests that eddies entered at specific dates (Fig. 7). The time-series is compared with an estimation of the transport around the ZD (Fig. 7). Using satellite altimetry data for the period 1993–2006, Saraceno et al. (2009) showed that the 4-year low-pass-filtered transport time-series associated with the ZD had a local minimum during the years 1998–2003. We extended the transport estimation to compare it with the time-series of the number of C eddies that enter the ZD area produced in this work (Fig. 7). The comparison suggests that when the low-frequency component of the transport associated with the ZD is less than 25 Sverdrups, more eddies are able to enter the ZD area and, when the transport is larger than 25 Sverdrups, fewer C eddies enter the ZD area. On the other hand, the non-filtered transport time-series (not shown) does not significantly correlate at any time lag with the number of C eddies inside the ZD area. While the low-frequency transport may affect the distribution of eddies, an instantaneous response is not necessarily expected. In other words, the foregoing results suggest that the low-frequency component of the transport of the anticyclonic current associated with the ZD may be associated with the number of C eddies inside the ZD area, whereas this is not observed at higher frequencies.

The yearly average temporal distribution of A eddies that entered the ZD area (18 in total) shows that a maximum of three eddies per year entered during the years 2003 and 2007, whereas during the other years a maximum of two eddies per year entered (not shown). The low number of A eddies does not allow any robust statistical analysis. Furthermore, trajectories of long-lived eddies (Fig. 6) suggest that A eddies that entered the ZD area dissipated very quickly.

5. Summary and discussion

Eddies in the southwestern Atlantic are detected from satellite altimetry data using a modified version of the OW method. Distribution of eddies in the region shows two salient observations: (i) the number of C eddies detected inside the ZD area is ten times larger than the number of A eddies; and (ii) a larger number of A eddies were detected just outside the ZD area. We proposed that perturbations of the A circulation associated with the ZD may generate meanders which, when occurring inside the ZD area, could detach from the main current and generate a C eddy (Fig. 4). A similar mechanism may explain the higher number of A eddies observed outside the ZD area.

The absence of A eddies inside the ZD anticyclone is a strong indication that meandering is occurring. Although very few anticyclonic eddies made their way to the center of the ZD region, this happened when the associated circulation was at its weakest (Fig. 7) and indicates the key role of the mean anticyclonic Zapiola Current in selecting what type of eddies can enter the ZD anticyclone.

However, another explanation for a preference for cyclonic eddies near the ZD is linked to the conservation of potential vorticity, assuming that bottom friction is weak. Indeed a vorticity anomaly traveling upslope would need to decrease its relative vorticity, so that anticyclonic eddies would weaken, whereas cyclonic eddies would be reinforced on their way towards the ZD center. Fig. 6 supports this mechanism, since it shows that anticyclones quickly disappear after entering the ZD area.

The preferred path for C eddies to enter the ZD area is the northeastern side of the region, where the potential vorticity gradient is lower compared to other sides (Fig. 5). Thus, the distribution of eddies described in this work is coherent with an anticyclonic ZD circulation that might meander and release more eddies on the northeastern side of the region.

As the elevation of the ZD results in a selection mechanism to filter A eddies, we could anticipate that a similar result should occur in other places with similar characteristics. In the North Atlantic, the Azores Plateau (AP) is an anomaly of the Mid-Atlantic Ridge (MAR), located approximately at 40°N, 30°W. The AP appears as a local topographic elevation of roughly 1200 m altitude relative to the MAR, and a lateral extent of 1500 km in both the meridional and zonal directions, and therefore with similar characteristics to the ZD. Evidence also exists that there is an anticyclonic gyre over the AP (Klein and Seidler 1989; Pollard et al., 1996), but of one to two orders of magnitude lower intensity in transport compared to the anticyclonic ZD Current (100 Sv, according to Saunders and King (1995a). Since we do not estimate eddies in the AP region, we compared eddy censuses in both the ZD and AP regions by looking at figures from Chelton et al. (2011a). Their Figs. 4(a) and 8 clearly show that more cyclonic than anticyclonic eddies entered the ZD region, as we illustrated in the present article. A white spot coincident with the AP region is visible in their Fig. 4a (Chelton et al., 2011a), clearly suggesting the bathymetric forcing. However, no predominance of a given eddy polarity is observed in the AP region (their Fig. 8). This may be due to the difference in strength of the two anticyclonic currents associated with the seabed elevations.

The prospects for continuing the work presented here include a study of the contribution of eddies to an explanation of the spatio-temporal distribution of chlorophyll-*a* in the southwestern Atlantic. As a preliminary result, Fig. 8 shows that the average

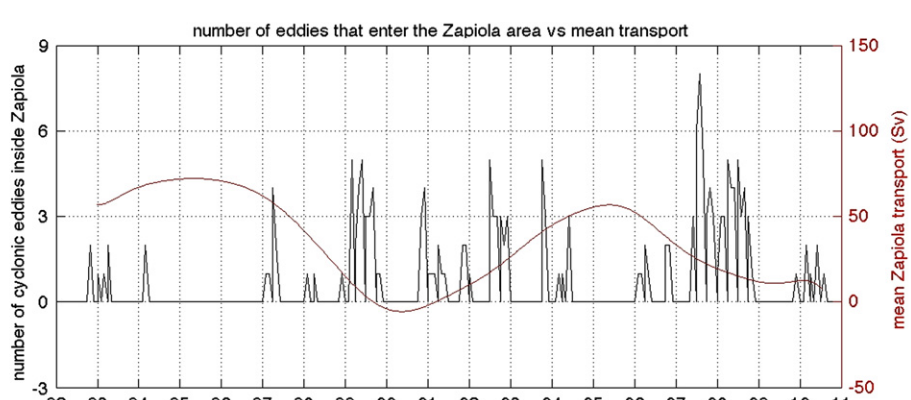

Fig. 7. Number of cyclonic eddies inside the ZD area (*black line*) and a 4-year low-pass-filtered transport time-series associated with the Zapiola Current (*red line*, units Sverdrups, 1 Sverdrup $=10^6$ m^3 s^{-1}). (For interpretation of the references to color in this figure legend, the reader is referred to the web version of this article.)

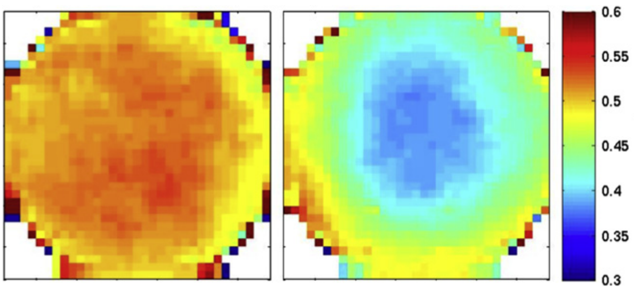

Fig. 8. Composite average of chlorophyll-*a* concentration within cyclonic (left panel) and anticyclonic (right panel) eddy interiors in a translating and normalized coordinate system. Only eddies with more than 50% of pixels without clouds have been considered.

surface chlorophyll-*a* concentration in C eddies is higher than that in A eddies. Thus, on average, the classical eddy pumping theory, i.e., uplift of the upper thermocline inside the eddy to bring nutrients into the euphotic zone (e.g., McGillicuddy et al., 1998; Siegel et al., 1999), explains the difference in chlorophyll-*a* concentration in the two types of eddies in the SWA. However, careful inspection of the different mechanisms (e.g., eddy pumping, eddy advection, wind-forced Ekman pumping and submesoscale effects) that might explain the spatio-temporal distribution of the chlorophyll-*a* concentration forced by the eddies is necessary before assessing which mechanism makes the largest contribution. Given the wide range of eddy energy (e.g., $10^2 - 2 \times 10^3$ cm^2 s^{-2}) and the sharp contrasts in chlorophyll-*a* concentration (0.05–10 mg m^{-3}), the SWA is a useful region to test the role of eddies in the chlorophyll-*a* distribution in different environments.

Acknowledgments

The altimeter products were produced by Ssalto/Duacs and distributed by AVISO, with support from CNES (http://www.aviso.oceanobs.com/duacs/). U. Zajaczkovski helped with the selection of the drifter data. D. Oks contributed to the computation of data for Fig. 8. This work is a contribution to projects ANPCyT PICT 2009–27, IAI CRN2076, CONICET PIP 112-200801-03072 and UBACYT 2008 × 176. CNES support is acknowledged. We warmly thank Ray Griffiths for his most valuable comments on the manuscript.

References

Acha, E.M., Mianzan, H.W., Guerrero, R.A., Favero, M., Bava, J., 2004. Marine fronts at the continental shelves of austral South America—physical and ecological processes. J. Mar. Syst. 44, 83–105.

Barré, N., Provost, C., Saraceno, M., 2006. Spatial and temporal scales of the Brazil Malvinas Current confluence documented by simultaneous MODIS aqua 1.1-km resolution SST and color images. Adv. Space Res. 37, 770–786.

Bigorre, S., Dewar, W.K., 2009. Oceanic time variability near a large scale topographic circulation. Ocean Modell. 29 (3), 176–188.

Chaigneau, A., Gizolme, A., Grados, C., 2008. Mesoscale eddies off Peru in altimeter records: identification algorithms and eddy spatio-temporal patterns. Prog. Oceanogr. 79 (2-4), 106–119.

Chaigneau, A., Eldin, G., Dewitte, B., 2009. Eddy activity in the four major upwelling systems from satellite altimetry (1992–2007). Prog. Oceanogr. 83 (1-4), 117–123.

Chelton, D.B., Schlax, M.G., Samelson, R.M., 2011a. Global observations of nonlinear mesoscale eddies. Prog. Oceanogr. 91 (2), 167–216.

Chelton, D.B., Schlax, M.G., Witter, D.L., Richman, J.G., 1990. Geosat altimeter observations of the surface circulation of the Southern ocean. J. Geophys. Res. 95 (C10), 17,877–17,903.

Dewar, W.K., 1998. Topography and barotropic transport control by bottom friction. J. Mar. Res. 56 (2), 295–328.

Farneti, R., Delworth, T.L., Rosati, A.J., Griffies, S.M., Zeng, Fanrong, 2010. The role of mesoscale eddies in the rectification of the Southern ocean response to climate change. J. Phys. Oceanogr. 40, 1539–1557, http://dx.doi.org/10.1175/2010JPO4353.1.

Fu, L.L., Cazenave, A., 2001. Satellite Altimetry and the Earth Sciences: A Handbook of Techniques and Applications. Academic Press, San Diego, CA. 463pp.

Garver, S.A., Siegel, D.A., 1997. Inherent optical property inversion of ocean color spectra and its biogeochemical interpretation: 1. Time series from the Sargasso Sea. J. Geophys. Res. 102, 18,607–18,625.

Gordon, A.L., 1981. South Atlantic thermocline ventilation. Deep-Sea Res. I. Oceanographic Research Papers 28 (11), 1239–1264.

Hansen, D.V., Poulain, P.M., 1996. Quality control and interpolations of WOCE-TOGA drifter data. J. Atmos. Oceanic Technol. 13, 900–909.

Isern-Fontanet, J., García-Ladona, E., Font, J., 2003. Identification of marine eddies from altimetry. J. Atmos. Oceanic Technol. 20, 772–778.

Klein, B., Seidler, G., 1989. On the origin of the Azores Current. J. Geophys. Res. 94, 6159–6168.

Le Traon, P.Y., Faugere, Y., Hernandez, F., Dorandeu, J., Mertz, F., Ablain, M., 2003. Can we merge GEOSAT follow-on with TOPEX/Poseidon and ERS-2 for an improved description of the ocean circulation? J. Atmos. Oceanic Technol. 20, 889–895.

Legeckis, R., Gordon, A.L., 1982. Satellite observations of the Brazil and Falkland Currents—1975 to 1976 and 1978. Deep-Sea Res. I—Oceanographic Research Papers 29 (3), 375–401.

Lentini, A.D., Goni, G.J., Olson, D.B., 2006. Investigation of Brazil Current rings in the confluence region. J. Geophys. Res. 111, C06013, http://dx.doi.org/10.1029/2005JC002988.

Maritorena, S., Siegel, D.A., Peterson, A., 2002. Optimization of a semi-analytical ocean color model for global scale applications. Remote Sens. Environ. 94, 429–440.

Mazloff, M.R., Heinback, P., Wunsch, C., 2010. An eddy-permitting Southern Ocean state estimate. J. Phys. Oceanogr. 40, 880–899.

McClain, C.R., Cleave, M.L., Fledman, G.C., Gregg, W.W., Hooker, S.B., Kurig, N., 1998. Science quality SeaWiFS data for global biosphere research. Sea Technol. 39, 10–16.

McGillicuddy Jr., D.J., Robinson, A.R., Siegel, D.A., Jannasch, H.W., Johnson, R., Dickey, T.D., McNeil, J., Michaels, A.F., Knap, A.H., 1998. Influence of mesoscale eddies on new production in the Sargasso Sea. Nature 394, 263–266, http://dx.doi.org/10.1038/28367.

Okubo, A., 1970. Horizontal dispersion of floatable particles in the vicinity of velocity singularities such as convergences. Deep-Sea Res. 17, 445–454.

Penven, P., Echevin, V., Pasapera, J., Colas, F., Tam, J., 2005. Average circulation, seasonal cycle, and mesoscale dynamics of the Peru Current system: a modeling approach. J. Geophys. Res., Oceans 110, C10021 , http://dx.doi.org/10.1029/ 2005JC002945.

Pollard, R., Griffiths, M., Cunningham, S., Read, J., Perez, F., Rios, A., 1996. Vivaldi, 1991: a study of the formation, circulation and ventilation of Eastern North Atlantic Central Water. Prog. Oceanogr. 37, 167–192.

Pascual, A., Faugere, Y., Larnicol, G., Le Traon, P.-Y., 2006. Improved description of the ocean mesoscale variability by combining four satellite altimeters. Geophys. Res. Lett. 33, 02611.

Peterson, R.G., Stramma, L., 1991. Upper-level circulation in the South Atlantic Ocean. Prog. Oceanogr. 26 (1), 1–73.

Ralph, E.A., Niiler, P.P., 1999. Wind-driven currents in the tropical Pacific. J. Phys. Oceanogr. 29 (9), 2121–2129.

Saraceno, M., Provost, C., Piola, A.R., Bava, J., Gagliardini, A., 2004. Brazil Malvinas frontal system as seen from 9 years of advanced very high resolution radiometer data. J. Geophys. Res. 109, C05027.

Saraceno, M., Provost, C., Piola, A.R., 2005. On the relationship between satellite-retrieved surface temperature fronts and chlorophyll-*a* in the western South Atlantic. J. Geophys. Res., C: Oceans 110 (11), 1–16.

Saraceno, M., Provost, C., Zajaczkovski, U., 2009. Long-term variation in the anticyclonic ocean circulation over the Zapiola Rise as observed by satellite altimetry: Evidence of possible collapses. Deep-Sea Res. I: Oceanographic Research Papers 56 (7), 1077–1092.

Saraceno, M., 2010. Mesoscale variability in the Brazil/Malvinas confluence region revisited. EOS Trans. AGU, Meet. Am. Suppl. 91 (26), 851231, Abstract.

Siegel, D.A., Fields, E., McGillicuddy Jr., D.J., 1999. Mesoscale motions, satellite altimetry and new production in the Sargasso Sea. J. Geophys. Res. 104, 13,359–13,379 , http://dx.doi.org/10.1029/1999JC900051.

Saunders, P., King, B.A., 1995a. Bottom current derived from a shipborne ADCP on WOCE cruise A11 in the South Atlantic. J. Phys. Oceanogr. 25, 329–347.

Saunders, P.M., King, B.A., 1995b. Oceanic fluxes on the WOCE A11 section. J. Phys. Oceanogr. 25 (9), 1942–1958.

Schmitz, W.J., Holland, W.R., 1982. A preliminary comparison of selected numerical eddy-resolving general-circulation experiments with observations. J. Mar. Res. 40 (1), 75–117.

Venaille, A., Le Sommer, J., Molines, J.-M., Barnier, B., 2011. Stochastic variability of oceanic flows above topography anomalies. Geophys. Res. Lett. 38, L16611, http://dx.doi.org/10.1029/2011GL048401.

Weiss, J., 1991. The dynamics of enstrophy transfer in two-dimensional hydrodynamics. Physica D 48, 273–294.